JOURNAL OF COMPUTATIONAL PHYSICS 109, 169–192 (1993)

Direct Numerical Simulation of Transition and Turbulence in a Spatially Evolving Boundary Layer

MAN MOHAN RAI

NASA Ames Research Center, Moffett Field, California 94035

AND

PARVIZ MOIN

Stanford University, Stanford, California 94305 and NASA Ames Research Center, Moffett Field, California 94035

Received June 15, 1992

A high-order-accurate finite-difference approach to direct simulations of transition and turbulence in compressible flows is described. The technique involves using a zonal grid system, upwind-biased differences for the convective terms, central differences for the viscous terms, and an iterative-implicit time-integration scheme. The integration method is used to compute transition and turbulence on a flat plate. The main objective is to determine the computability of such a flow with currently available computer speeds and storage and to address some of the algorithmic issues such as accuracy, inlet and exit boundary conditions, and grid-point requirements. A novel feature of the present study is the presence of high levels of broad band freestream fluctuations. The computed data are in qualitative agreement with experimental data (from experiments on which the computation is modeled). The computational results indicate that the essential features of the transition process have been captured. Additionally, the finite-difference method presented in this study can, in a straightforward manner, be used for complex geometries.

INTRODUCTION

In recent years the techniques of computational fluid dynamics (CFD) have been used to compute flows associated with geometrically complex configurations. However, success in terms of accuracy and reliability has been limited to cases in which the effects of turbulence and transition could be modeled in a straightforward manner. Even in simple flows, the accurate computation of skin friction and heat transfer using existing turbulence models has proved to be a difficult task, one that requires extensive fine-tuning of the constants in the turbulence models used. In complex flows (for example, in turbomachinery flows in which vortices and wakes impinge on airfoil surfaces causing periodic transition from laminar to turbulent flow), the development of a turbulence model that accounts for all scales of turbulence and predicts the onset of transition may prove to be impractical.

Fortunately, current trends in computing suggest that it may be possible to perform direct simulations of turbulence and transition at moderate Reynolds numbers in some complex cases in the near future.

In this paper we report on a direct simulation of transition and turbulence in a spatially evolving boundary layer on a flat plate. This flows exhibits laminar, transitional, and turbulent characteristics and, hence, is a test case that has many of the characteristics found in more complex flows. The main objective of the study is to determine the computability of such a flow with currently available computer speeds and storage and to address some of the algorithmic issues such as accuracy, inlet and exit boundary conditions, and grid-point requirements. A study of the fluid physics involved and the creation of a data base for turbulence and transition modeling are an integral part of this effort.

Most of the earlier work in direct simulations of transition has been confined to the temporal evolution of a boundary layer that is subject to certain initial disturbance fields. Reference [1] presents one such direct simulation that is tailored to mirror the experimental data of Ref. [2]. The incompressible form of the Navier–Stokes equations was solved using a spectral method in the streamwise and spanwise directions and a second-order-accurate central-difference method in the wall-normal direction. The computed physical phenomena such as detached shear layers and spikes in the "peak plane" were found to be in good agreement with the experimental measurements.

* Originally presented as AIAA Paper No. 91-1607 at the "AIAA 10th Computational Fluid Dynamics Conference, Honolulu, Hawaii, June 24–26, 1991."

0021-9991/93 $5.00

581/109/2-2

Reference [3] also describes direct simulations of a temporally evolving boundary layer. As in Ref. [1], the computation is performed using a parallel mean-flow assumption that permits the use of a Fourier spectral method in the streamwise and spanwise directions. Whereas, a two-dimensional eigensolution and a pair of oblique three-dimensional eigensolutions of the Orr–Sommerfeld equation were used as the initial perturbation in Ref. [1], a finite-amplitude two-dimensional eigensolution of the Orr–Sommerfeld equation and low-amplitude, three-dimensional random noise were used in Ref. [3]. The advantage of the latter approach is that the dominant spanwise wave number emerges from the computation instead of being assumed as was done in Ref. [1]. Reference [4] presents a numerical investigation that is similar to those of Refs. [1, 3]. The incompressible form of the Navier–Stokes equations is solved with a parallel flow assumption and with periodic boundary conditions in the streamwise and spanwise directions. A Fourier spectral method is used in the streamwise and spanwise directions, and a Chebyshev collocation method is used in the wall-normal direction. Studies of both the Klebanoff-type and subharmonic-type of transition are presented.

Clearly, studies of the temporal evolution of boundary layers have both increased our understanding of transition and yielded estimates of the computing requirements for direct simulations of transition. However, those studies were approximations to a spatially evolving boundary layer. A numerical investigation of the growth of instabilities in a spatially evolving boundary layer is presented in Ref. [5]. The incompressible form of the Navier–Stokes equations is solved using fourth-order accurate finite-differences in the streamwise and wall-normal directions and a Fourier spectral method in the spanwise direction. The governing equations are solved by using a vorticity–velocity formulation for the disturbance variables. The disturbances are introduced into the flow field by means of blowing and suction over a portion of the upstream region of the flat plate. Results are presented for the spatial evolution of small-amplitude disturbances, subharmonic resonance breakdown, and fundamental resonance breakdown. However, the computations are limited to the onset of transition.

Here we present results obtained for a spatially evolving (flat-plate) boundary layer. The computational region includes both the transition region and the turbulent region. A direct simulation of low free-stream disturbance transition that includes both the transition and turbulent regions would require far greater computational resources than are currently available. A recent investigation [6] reports on the pitfalls of inadequate resolution in simulating transitional flows. However, for high levels of free-stream turbulence the transition region is much closer to the leading edge of the flat plate, and hence it may be computable on currently available computers. In this study we attempt one such simulation that is modeled on the experiments reported in Refs. [7–9]. The free-stream turbulence intensity in these experiments is approximately 2.6%, the onset of transition is at roughly $Re_x = 250{,}000$, and the flow becomes fully turbulent around $Re_x = 600{,}000$ (Re_x is the Reynolds number based on the length of the plate).

One of the advantages of the parallel flow assumption is that periodic boundary conditions can be used in the streamwise direction (in addition to periodicity in the spanwise direction) and, consequently, the highly accurate Fourier spectral approach can be used in both the spanwise and streamwise directions. Obviously, such an assumption cannot be made in the general case. Reference [10] presents a high-order accurate, upwind-biased, finite-difference scheme for the incompressible form of the Navier–Stokes equations. This scheme was developed to investigate the possibility of performing direct simulations of turbulent and transitional flow in general geometries with arbitrary boundary conditions in an efficient and straightforward manner. The scheme was used to compute the exponential growth of two-dimensional eigensolutions of the Orr–Sommerfeld equation, as well as to compute the fully developed turbulent flow in a channel. The growth rate of the eigensolution agreed very well with that predicted by linear theory. The turbulent channel-flow simulation yielded mean flow properties and higher-order turbulence statistics that agreed well with both experimental data and earlier spectral simulations (with approximately the same number of grid points).

In the present study the method of Ref. [10] is extended to solve the compressible form of the Navier–Stokes equations. Details regarding the scheme and the boundary conditions employed are described in the following sections. One additional feature that is included in the present formulation is the use of multiple zones in the computation; different zones contain different grid densities. Such a zonal approach makes the best possible use of computer resources and is thus essential to performing computationally intensive simulations such as those of transition and turbulence. The zonal method is also discussed in the following sections.

The results presented herein comprise velocity statistics and skin friction in the turbulent and transition regions, as well as the development of streamwise and spanwise vorticity fields in the transition region.

NUMERICAL METHOD

A finite-difference technique was used in Ref. [10] to obtain an accurate simulation of incompressible, fully developed, turbulent channel flow. The computed turbulence statistics were in good agreement with those obtained using a spectral method with approximately the

same number of grid points. The finite-difference technique used in Ref. [10] is based on a partially implicit, fractional-step method developed in Ref. [11].

One of the problems encountered in direct simulations of turbulent flow is the control of aliasing errors. The use of schemes that do not have a mechanism for controlling such errors can result in the decay of the turbulence in a given flow field or an unbounded growth of the solution in others. One method of reducing the effect of this problem is to use kinetic-energy conserving schemes. Energy is conserved by such schemes, but it is not clear how that energy is redistributed. A second method of controlling aliasing error is to extract and discard at each time step that energy which would otherwise be aliased back. However, current procedures that perform this operation rely on series representations of the dependent variables (such as Fourier representations), and it is not clear how these procedures can be extended to curvilinear grids.

The method of Ref. [10] uses an upwind-biased differencing technique for the convective terms of the Navier–Stokes equations to control aliasing errors. The leading truncation-error term of some upwind differences is dissipative in nature and thus damps the higher-frequency content. The main disadvantage is that the useful information in the high-wave-number portion of the spectrum is also lost in the process. However, this problem can be overcome with the use of additional grid points. The upwind-biased finite-difference technique (like other finite-difference techniques) also has the advantage that it can be used for curvilinear grids in a straightforward manner.

The results of Ref. [10] clearly demonstrate that significant reductions in the number of grid points can be obtained with the use of high-order-accurate differencing techniques. The method of Ref. [10] uses fifth-order-accurate upwind-biased differences for the convective terms and sixth-order-accurate central differences for the viscous terms. It can be shown that $2n+1$ grid points are required to produce nth-order-accurate fully upwind differences (this estimate takes into account that both forward and backward differences of a given quantity may be required at any grid point). Thus an 11-point stencil is required in order to produce fifth-order-accurate upwind differences. The problem with such large stencils is that many grid points near the computational boundaries can no longer be treated using the finite differences used in the interior; therefore, they will require special treatment. Hence, finite differences are needed that are as compact as possible, subject to the constraint that they have the desirable damping that controls aliasing errors.

Upwind-biased differences require a much smaller stencil than fully upwind differences in order to obtain a given order of accuracy and, in addition, have the desired dissipation to control aliasing error. Upwind-biased differences achieve a higher order of accuracy for a given stencil size by using grid points on either side of the point in question, but with more points in the direction in which the difference is to be biased. For example, a decision to use at most five grid points (two on either side of the point at which the derivative is to be calculated) would result in a second-order-accurate fully upwind (backward) difference for a first derivative,

$$\left(\frac{\partial u}{\partial x}\right)_j = \frac{3u_j - 4u_{j-1} + u_{j-2}}{2\Delta x},$$

whereas the same derivative could be computed to third-order accuracy using upwind-biased differences as follows:

$$\left(\frac{\partial u}{\partial x}\right)_j = \frac{2u_{j+1} + 3u_j - 6u_{j-1} + u_{j-2}}{6\Delta x}.$$

The use of the entire stencil would result in a fourth-order-accurate central difference without natural dissipation. The method of Ref. [10] uses a seven-point stencil to obtain fifth-order-accurate, biased backward and forward differences.

The integration method used in this study for the compressible form of the Navier–Stokes equations incorporates all of the features discussed above. The present method is a high-order-accurate, upwind-biased, finite-difference technique that is used in conjunction with an iterative-implicit time-advancement scheme. The convective terms are evaluated as in Ref. [12] (but with high-order-accurate differences instead of second-order-accurate differences), and the iterative implicit technique of Ref. [13] is used to integrate the equations of motion in time.

To describe the method, we consider the unsteady, compressible, nonconservative formulation of the Navier–Stokes equations in three spatial dimensions,

$$Q_t + AQ_x + BQ_y + CQ_z = \frac{1}{\rho}(R_x + S_y + T_z), \qquad (1)$$

where Q is the vector of dependent variables

$$Q = \begin{pmatrix} \rho \\ u \\ v \\ w \\ p \end{pmatrix}. \qquad (2)$$

In Eq. (2), ρ is the density; u, v, and w are the velocities in

the x, y, and z directions, respectively; and p is the pressure. The matrices A, B, and C are obtained from the matrix D,

$$D=\begin{pmatrix} q & k_1\rho & k_2\rho & k_3\rho & 0 \\ 0 & q & 0 & 0 & k_1/\rho \\ 0 & 0 & q & 0 & k_2/\rho \\ 0 & 0 & 0 & q & k_3/\rho \\ 0 & k_1\gamma p & k_2\gamma p & k_3\gamma p & q \end{pmatrix}, \tag{3}$$

where q is defined as $q=uk_1+vk_2+wk_3$. The matrix A is obtained from D with $k_1=1$, $k_2=0$, and $k_3=0$; the matrix B is obtained with $k_1=0$, $k_2=1$, and $k_3=0$; and the matrix C is obtained using $k_1=0$, $k_2=0$, and $k_3=1$. The viscous term R_x on the right-hand side of Eq. (1) is given by

$$R_x=\begin{pmatrix} 0 \\ (2\mu u_x+\lambda(u_x+v_y+w_z))_x \\ (\mu(u_y+v_x))_x \\ (\mu(u_z+w_x))_x \\ \rho(\mu Pr^{-1}(c^2)_x)_x+\phi \end{pmatrix}, \tag{4}$$

where c is the local speed of sound and

$$\begin{aligned} \lambda &= -2\mu/3 \\ \phi &= \rho(\gamma-1)(u_x(2\mu u_x+\lambda(u_x+v_y+w_z)) \\ &\quad + v_x(\mu(u_y+v_x))+w_x(\mu(u_z+w_x))). \end{aligned} \tag{5}$$

The viscous terms S_y and T_z are obtained from similar expressions.

Before describing the time-integration method, it is helpful to consider the techniques used to compute the convective and viscous terms. The convective terms AQ_x, BQ_y, and CQ_z (Eq. (1)) are evaluated as in Ref. [12]. To illustrate the technique, we consider the term AQ_x. The matrix A can be written as

$$A=P\Lambda P^{-1} \tag{6}$$

where P^{-1} is the matrix of the left eigenvectors of A, and Λ is a diagonal matrix containing the eigenvalues of A. The term AQ_x is evaluated as

$$AQ_x=A^+Q_x^-+A^-Q_x^+ \tag{7}$$

where $A^\pm=P\Lambda^\pm P^{-1}$, and Λ^+ and Λ^- are diagonal matrices containing the positive and negative eigenvalues of A, respectively. The terms Q_x^+ and Q_x^- are forward and backward differences of the vector Q, respectively. Additional details regarding this method of evaluating the convective terms can be found in Ref. [12]. In the present study, Q_x^+ and Q_x^- are computed using fifth-order-accurate forward- and backward-biased finite differences using a seven-point stencil as

$$Q_x^-=\frac{\begin{pmatrix}-6Q_{i+2}+60Q_{i+1}+40Q_i \\ -120Q_{i-1}+30Q_{i-2}-4Q_{i-3}\end{pmatrix}}{120\Delta x}$$

$$Q_x^+=\frac{\begin{pmatrix}4Q_{i+3}-30Q_{i+2}+120Q_{i+1} \\ -40Q_i-60Q_{i-1}+6Q_{i-2}\end{pmatrix}}{120\Delta x}$$

on a grid that is equispaced in the x-direction. The remaining convective terms are evaluated in a similar manner. For stretched meshes (for example, the type used in the wall-normal direction in this study), the coefficients in the difference formulas are evaluated numerically using Lagrange polynomials so as to retain high-order accuracy even on grids where the rate of change of grid spacing is not sufficiently smooth (obtaining explicit formulas for these coefficients is a laborious task for differences with higher than second-order accuracy). Additional details regarding this procedure can be found in Ref. [10].

The viscous terms are computed using central differences and a five-point stencil (fourth-order accuracy). To illustrate, we consider the term $(\mu(u_y+v_x))_x$ in the vector R_x. This term is first expanded as

$$(\mu(u_y+v_x))_x=\mu_x(u_y+v_x)+\mu(u_{xy}+v_{xx}). \tag{8}$$

Each of the derivatives on the right-hand side of Eq. (8) is then evaluated using central differences. As in the case of the convective terms, the coefficients in the difference formulas are evaluated numerically using Lagrange polynomials.

The fully implicit finite-difference representation of Eq. (1) can now be written as

$$\begin{aligned} &\frac{3Q^{n+1}-4Q^n+Q^{n-1}}{2\Delta t} \\ &\quad +(A^+Q_x^-+A^-Q_x^+ + B^+Q_y^- \\ &\quad +B^-Q_y^+ + C^+Q_z^- + C^-Q_z^+)^{n+1} \\ &\quad =\left(\frac{1}{\rho}(R_x+S_y+T_z)\right)^{n+1} \end{aligned} \tag{9}$$

Equation (9) is second-order accurate in time and represents a system of nonlinear equations. This system of nonlinear equations can be solved using a Newton–Raphson-type iterative technique at each time step. The linearization of Eq. (9) results in

$$\left(1.5I+\Delta t\left(\frac{A^+\nabla_x}{\nabla x_i}+\frac{A^-\Delta_x}{\Delta x_i}\right)\right.$$
$$+\Delta t\left(\frac{B^+\nabla_y}{\nabla y_j}+\frac{B^-\Delta_y}{\Delta y_j}-M\left(\frac{\Delta_y}{\Delta y_j}+\frac{\nabla_y}{\nabla y_j}\right)\right.$$
$$\left.\left.-N\left(\frac{\Delta_y}{\Delta y_j}-\frac{\nabla_y}{\nabla y_j}\right)\right)\right.$$
$$\left.+\Delta t\left(\frac{C^+\nabla_z}{\nabla z_k}+\frac{C^-\Delta_z}{\Delta z_k}\right)\right)^p(Q^{p+1}-Q^p)$$
$$-\Delta t\left(\frac{3Q^p-4Q^n+Q^{n-1}}{2\Delta t}\right.$$
$$+(A^+Q_x^-+A^-Q_x^++B^+Q_y^-$$
$$+B^-Q_y^++C^+Q_z^-+C^-Q_z^+)^p$$
$$\left.-\left(\frac{1}{\rho}(R_x+S_y+T_z)\right)^p\right), \tag{10}$$

where ∇ and Δ are backward and forward difference operators, respectively, the matrices M and N represent the linearization of the first and second derivatives in the viscous terms, and p is an iteration index. For the viscous terms, only the derivatives in the y or wall-normal direction have been retained on the left-hand side (LHS). On the LHS of Eq. (10), the convective terms are represented with first-order-accurate formulations and the viscous terms with second-order formulations as in Ref. [13]. The reason this does not affect the accuracy of the scheme is as follows. In Eq. (10), Q^p is an approximation to Q^{n+1}. When $p=0$, $Q^p=Q^n$, and when Eq. (10) is iterated to convergence at a given time-step, $Q^p\to Q^{n+1}$. Since the LHS of Eq. (10) can be driven to zero at each time-step, linearization errors (such as those mentioned above) can be driven to zero during the iteration process. It should be noted that the discretization presented in Eq. (10) is valid only for rectangular grids (however, the grid spacing in each direction may vary).

The LHS of Eq. (10) represents a sparse matrix of large bandwidth and, therefore, is computationally expensive to solve. Reference [13] uses an approximate factorization technique, as was done in Ref. [14], to overcome this problem. The factored form of Eq. (10) is given by

$$\left(\alpha I+\beta\,\Delta t\left(\frac{A^+\nabla_x}{\nabla x_i}+\frac{A^-\Delta_x}{\Delta x_i}\right)\right)^p$$
$$\times\left(\alpha I+\beta\,\Delta t\left(\frac{B^+\nabla_y}{\nabla y_j}+\frac{B^-\Delta_y}{\Delta y_j}\right.\right.$$
$$\left.\left.-M\left(\frac{\Delta y}{\Delta y_j}+\frac{\nabla_y}{\nabla y_j}\right)-N\left(\frac{\Delta_y}{\Delta y_j}-\frac{\nabla_y}{\nabla y_j}\right)\right)\right)^p$$
$$\times\left(\alpha I+\beta\,\Delta t\left(\frac{C^+\nabla_z}{\nabla z_k}+\frac{C^-\Delta_z}{\Delta z_k}\right)\right)^p(Q^{p+1}-Q^p)$$
$$=-\Delta t\left(\frac{3Q^p-4Q^n+Q^{n-1}}{2\Delta t}\right.$$
$$+(A^+Q_x^-+A^-Q_x^++B^+Q_y^-$$
$$+B^-Q_y^++C^+Q_z^-+C^-Q_z^+)^p$$
$$\left.-\left(\frac{1}{\rho}(R_x+S_y+T_z)\right)^p\right), \tag{11}$$

where $\alpha=1.5^{1/3}$ and $\beta=1.5^{-2/3}$. The approximation made earlier of using a three-point stencil in formulating the LHS of Eq. (10) has resulted in systems of block-tridiagonal matrices in Eq. (11) instead of block-heptadiagonal matrices; this reduces the computing time required at each iteration at the possible expense of the number of iterations to converge. The factorization error, just like the linearization error, can be driven to zero during the iteration process.

One additional approximation that has been made to the x and z terms on the LHS of Eq. (11) is the use of diagonal forms as in Ref. [15]. The inversion in the x direction is approximated as

$$\left(\alpha I+\beta\,\Delta t\left(\frac{A^+\nabla_x}{\nabla x_i}+\frac{A^-\Delta_x}{\Delta x_i}\right)\right)$$
$$\simeq P\left(\alpha I+\beta\,\Delta t\left(\frac{A^+\nabla_x}{\nabla x_i}+\frac{A^-\Delta_x}{\Delta x_i}\right)\right)P^{-1}, \tag{12}$$

where the matrices P, P^{-1}, and Λ are defined in Eq. (6). This approximation results in systems of scalar tridiagonal equations instead of systems of block-tridiagonal equations. The inversion in the z direction is treated in a similar manner. The use of the diagonal form of the equations resulted in a decrease of about 25% in computation time. The diagonalized form was not used in the y direction because of the presence of the viscous terms.

An important limitation imposed by using the nonconservative formulation of the Navier–Stokes equations is that the method can only be used to compute flows that are free of flow discontinuities (such as purely subsonic flows). The nonconservative formulation of the governing equations has been chosen for this investigation because the associated finite-difference method can, in a straightforward manner, be extended to curvilinear coordinate systems without a loss in accuracy. Methods that use the conservative form of the equations, that are conservative in a discrete sense, and that are high-order accurate on generalized grids are still under development. In summary, the present method is second-order accurate in time and fourth-order accurate in space.

BOUNDARY CONDITIONS

The computational region of interest (Fig. 1) consists of three zones. Zone 1 is an inlet region where the "computed

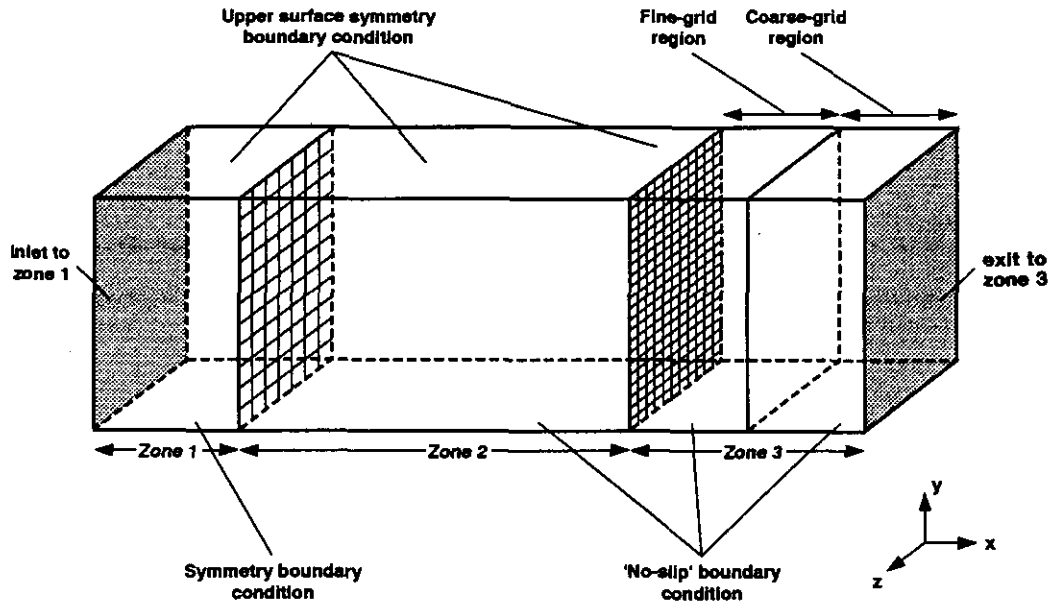

FIG. 1. Schematic of computational region (not to scale).

freestream turbulence" develops. This is followed by zone 2, whose upstream boundary is at the leading edge of the flat plate. Zone 3 occurs immediately downstream of zone 2 and contains the exit region where the grid becomes extremely coarse in the streamwise direction. The use of two separate zones to cover the flat plate permits the use of different grid densities in the regions comprising these zones. Typically, zone 3 contains the highest grid resolution of all the zones and is placed in the region that is to be studied in detail. Figure 2 shows the lengths of zones 1, 2, and 3 used in two different computations that are performed in this study.

The boundaries that contain the several grids that are used in this study can be broadly classified as natural boundaries and zonal boundaries. The natural boundaries include the inlet boundary of the first zone (which is also the inlet to the entire region), the lower surface boundaries of all three zones, the exit boundary of the third zone (which is also the exit to the entire region), the periodic boundaries in the spanwise (z) direction and the upper boundaries of all the three zones. The boundary between the first and second zones and the boundary between the second and third zones together comprise the zonal boundaries of the system. Both the natural and zonal boundary conditions are discussed in the following section.

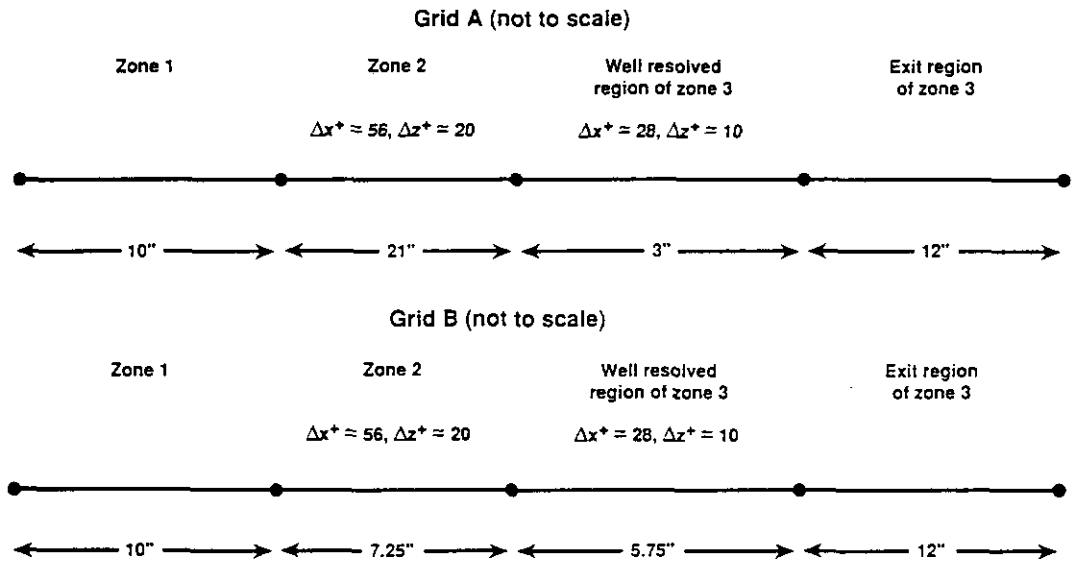

FIG. 2. Zonal configurations used in grids A and B.

Inlet Boundary of Zone 1

The inlet boundary of the first zone is a subsonic inlet boundary. Four quantities must be specified at this boundary. The four chosen for this study are a Riemann invariant $R_1 = u + 2c/(\gamma - 1)$, the stagnation pressure and the velocities in the wall-normal (y) and spanwise (z) directions. A second Riemann invariant $R_2 = u - 2c/(\gamma - 1)$ is extrapolated from the interior of zone 1 to complete the system of equations required to uniquely determine the dependent variables at the inlet. The resulting system of equations is given by

$$\begin{aligned} u_b + 2c_b/(\gamma-1) &= (u_\infty + \tilde{u}) + 2c_\infty/(\gamma-1) \\ u_b - 2c_b/(\gamma-1) &= u_2 - 2c_2/(\gamma-1) \\ v_b &= \tilde{v} \\ w_b &= \tilde{w} \\ p_b &= P_\infty \left(1 + \frac{\gamma-1}{2} \times \frac{(u_b^2 + v_b^2 + w_b^2)}{c_b^2}\right)^{-\gamma/(\gamma-1)}, \end{aligned} \tag{13}$$

where P is the stagnation pressure and where the subscripts b, ∞, and 2 refer to the boundary, inlet reference variables, and the grid point just downstream of the inlet boundary, respectively. The quantities $\tilde{u}$, $\tilde{v}$, and $\tilde{w}$ are prescribed velocity perturbations.

The perturbation velocities are computed using a prescribed value of the root-mean-square intensity, length scale, and range of frequencies over which the energy is to be distributed. The procedure used in this study is similar but not identical to that used in Ref. [16]. The describe this procedure we consider the perturbation velocity $\tilde{u}(y, z, t)$. Assuming periodicity in y, z, and t we can write the Fourier representation of $\tilde{u}(y, z, t)$,

$$\tilde{u}(y,z,t) = \sum_{l=1}^{L}\sum_{m=1}^{M}\sum_{n=1}^{N} A_{lmn} \sin\left(\frac{2\pi l y}{L_y} + \phi_l\right) \times \sin\left(\frac{2\pi m z}{L_z} + \phi_m\right) \sin\left(\frac{2\pi n t}{T} + \phi_n\right), \tag{14}$$

where L_y and L_z are the dimensions of the computational region in the y and z directions, respectively, T is the period of the lowest frequency to be generated, and the phase angles ϕ_l, ϕ_m, and ϕ_n are random numbers between zero and 2π. We now chose a simple form for the coefficients A_{lmn},

$$A_{lmn}^2 = 8u_{rms}^2 Y(l)\, Z(m)\, T(n), \tag{15}$$

where

$$\begin{aligned} Y(l) &= K_Y d_Y^{l-1}, \qquad l = 1, 2, ..., L, \\ Z(m) &= K_Z d_Z^{m-1}, \qquad m = 1, 2, ..., M, \end{aligned} \tag{16}$$

and the function $T(n)$ is assumed to satisfy the Von Karman spectrum; that is,

$$\begin{aligned} \frac{T(n+1)}{T(n)} &= \frac{1 + \theta^2 n^2}{1 + \theta^2 (n+1)^2} \\ \theta &= \frac{2\pi \Lambda}{U}. \end{aligned} \tag{17}$$

In Eq. (17), Λ is the longitudinal length scale, U is the mean freestream velocity, and n is the wavenumber. The values of the constants K_Y, K_Z, and $T(1)$ are chosen such that the conditions

$$\begin{aligned} \sum_{l=1}^{L} Y(l) &= 1 \\ \sum_{m=1}^{M} Z(m) &= 1 \\ \sum_{n=1}^{N} T(n) &= 1 \end{aligned} \tag{18}$$

are satisfied. The disturbances obtained at the exit of the first zone exhibit characteristics that are different from those specified at the inlet; these characteristics are presented later in the paper.

Lower Boundary of Zones 1–3

The lower boundary of the first zone is treated as a symmetry boundary, and the dependent variables at this boundary are determined from the following relationships:

$$\begin{aligned} \rho_1 &= \rho_2 \\ u_1 &= u_2 \\ v_1 &= 0 \\ w_1 &= w_2 \\ p_1 &= p_2, \end{aligned} \tag{19}$$

where the subscripts 1 and 2 refer to the point on the boundary and the point just in the interior, respectively. This first-order-accurate approach to implementing the symmetry boundary condition was chosen instead of a higher-order-accurate approach because it was found that the higher-order-accurate approach resulted in a more restrictive choice of time-step near the leading edge (which is a flow singularity).

The "no-slip" boundary condition together with an adiabatic-wall condition and zero-normal derivative of the

pressure are imposed on the lower surface of zones 2 and 3. The pressure derivative condition, the adiabatic wall condition, and the equation of state together yield

$$\frac{\partial \rho}{\partial n} = 0.$$

The equations used to update the boundary points on the wall are given by

$$\begin{aligned} \rho_1 &= \rho_2 \\ u_1 &= 0 \\ v_1 &= 0 \\ w_1 &= 0 \\ p_1 &= p_2. \end{aligned} \tag{20}$$

Higher-order-accurate representations of the pressure and density derivative conditions such as

$$\rho_1 = (4\rho_2 - \rho_3)/3$$
$$p_1 = (4p_2 - p_3)/3$$

were also used and found to yield nearly identical solutions, but resulted in a more restrictive choice of time-step.

Exit Boundary of Zone 3

The exit boundary of zone 3 is a subsonic exit boundary. One flow quantity must be specified at this boundary. In this study the exit static pressure is specified and the remaining variables are extrapolated from the interior of zone 3. This boundary condition has the advantage that, together with the stagnation pressure specification at the inlet, it uniquely determines the mass flow through the system. However, it reflects pressure waves back into the system. It should be noted that pressure reflections are also encountered in the experiments of Refs. [7–9].

The flow across the exit boundary consists of an inviscid core region (which comprises most of the area of this boundary) and the boundary layer. In the present computation, the static pressure from the inviscid region (in the vicinity of the boundary layer) is imposed within the boundary-layer region of the exit boundary. However, this approach is valid only when the pressure gradient in the wall-normal direction within the boundary layer is small (which is not the case at any given instant in an unsteady turbulent boundary layer). In order to circumvent this problem, the grid in the exit region is gradually coarsened in the steamwise direction (by a factor of about 160). This approach has been found to numerically dissipate most of the unsteadiness within the boundary layer and, in addition, eliminates the reflection of high-frequency pressure waves. The direct consequence of using this approach is that the boundary-layer flow in the downstream portion of zone 3 is not physically realistic. Additional details regarding the effect of the coarse grid on the flow field are presented later in the paper.

Other Natural Boundaries

The remaining boundary conditions include the periodic boundaries in the z direction and the symmetry boundary condition on the upper surface of zones 1, 2, and 3. Implementing the periodic boundary condition is straightforward. The symmetry boundary condition is implemented by creating temporary arrays of variables above the plane of symmetry such that the equations of motion can be integrated at grid points on the plane of symmetry. The dependent variables above the plane of symmetry are computed, using the symmetry principle, as

$$\begin{aligned} \rho_0 &= \rho_i \\ u_0 &= u_i \\ v_0 &= -v_i \\ w_0 &= w_i \\ p_0 &= p_i, \end{aligned} \tag{21}$$

where the subscript o refers to the point above the plane of symmetry and the subscript i refers to the corresponding point below the plane of symmetry.

Zonal Boundary Conditions

The zonal boundaries that separate zones 1 and 2 and zones 2 and 3 are treated by using an interpolation procedure that is explicit at each iteration within a given step but which is implicit over the entire time step. To describe the procedure in detail we consider the zonal boundary between zones 1 and 2. The grids in these zones are generated such that there is an area of overlap between the two grids. In addition, they are constructed such that the last streamwise (constant-x) plane of zone 1 corresponds to an interior (constant-x) plane of zone 2 and the first streamwise plane of zone 2 corresponds to an interior plane of zone 1. Since the number of grid points used in zones 1 and 2 in the y and z directions is typically not the same and since the grid-point spacing in the y direction is not the same in these zones, the grid points of zone 1 do not coincide with those of zone 2. A cubic interpolation procedure (fourth-order accuracy) is used to transfer data between the two zones.

In integrating the equations of motion using the iterative implicit scheme of Eq. (11), it is necessary to specify boundary conditions on the exit boundary of zone 1 in order to perform an inversion in the x direction. The boundary condition used in this study is given by

$$(Q^{p+1} - Q^p)_{zb} = 0, \tag{22}$$

where the subscript zb refers to the zonal boundary. A similar procedure is used at the inlet boundary of zone 2 and at the zonal boundary separating zones 2 and 3. Upon completing one iteration in all the zones, the dependent variables at the exit boundary of zone 1 are obtained by interpolating the dependent variables in zone 2 that lie on the plane that coincides with the exit plane of zone 1. A similar post-update corrective procedure is applied at all the zonal boundaries. A major advantage of the above procedure is that at each iteration the computations within the various zones are uncoupled. A boundary condition that does not uncouple the computations in the different zones would result in systems of equations that are not banded, a result of the grid-line discontinuities at the boundary (which makes the solution extremely expensive).

It should be emphasized that the boundary condition given by Eq. (22) is not equivalent to

$$(Q^{n+1} - Q^n)_{zb} = 0 \tag{23}$$

followed by a post-update corrective procedure. Equation (22) (in addition to Eq. (11) at the interior points) allows $(Q^{n+1} - Q^n)_{zb}$ to assume its proper value when the iteration process is carried to convergence. Both time accuracy and spatial accuracy consistent with the order of interpolation used are maintained at the zonal boundary by using Eq. (22). On the other hand, Eq. (23) represents a purely explicit boundary procedure, which would adversely affect temporal accuracy, and, which may affect the stability of the algorithm and thus require the use of smaller time steps.

EVOLUTION OF SMALL AMPLITUDE DISTURBANCES

The numerical method and boundary conditions discussed in the previous sections and the corresponding computer program were tested by studying the growth of two-dimensional, small amplitude disturbances in flat plate flow. This investigation closely resembles that of Ref. [5]. The inlet region (zone 1) is not used in these computations; instead, the inlet boundary condition given by Eq. (13) (with the perturbation velocities set to zero) is implemented at the plane corresponding to the leading edge of the plate. In addition, zone 3 is also not included in these computations; zone 2 comprises both the fine-grid region where the computations are accurate as well as a coarse-grid exit region where the disturbances are attenuated.

Two-dimensional small amplitude disturbances are introduced into the computational region through blowing and suction at the wall as in Ref. [5]. The wall-normal velocity at the wall in a small strip near the leading edge is prescribed as

$$v = Au_\infty v_w(x) \sin(2\pi\beta t)$$

$$v_w(x) = 4 \sin(\theta)(1 - \cos(\theta))/(27)^{1/2}$$

$$\theta = 2\pi(x - x_a)/(x_b - x_a),$$

where x_a and x_b are the steamwise locations of the beginning and the end of the blowing/suction strip, respectively, A is the amplitude of the imposed disturbance, and β is the temporal frequency of the disturbance. The Reynolds number based on inlet conditions is 50,800/in. (flow velocity of 98.5 ft/s, freestream temperature of 560°R). The corresponding Mach number is 0.0849. The location of the strip is given by $x_a = 1.787$ in. ($\mathrm{Re}_{x_a} = 90{,}780$) and $x_b = 2.230$ in. ($\mathrm{Re}_{x_b} = 113{,}285$). The temporal frequency β and amplitude A used in this computation were $(6000/2\pi)$ Hz and 0.0001, respectively. The above conditions are the same as those used in Ref. [5] (however, the computations of Ref. [5] included a three-dimensional disturbance component of the same magnitude, whereas the present computation is two-dimensional).

The well-resolved portion of zone 2 was 7.0 in. in the streamwise direction ($\mathrm{Re}_x = 355{,}600$). This region is followed by a coarse-grid region that is 12.0 in. in extent. The upper symmetry boundary was place 30 in. away from the wall. The results presented in here were obtained with 351 grid points in the streamwise direction (in the well-resolved portion) and 71 grid points in the wall-normal direction (stretched grid). The grid spacing in the x direction and at the wall in the y direction are 0.02 in. (0.341δ) and 0.001 in. (0.017δ), respectively (δ is the boundary layer thickness at $\mathrm{Re}_x = 355{,}600$). The corresponding values used in Ref. [5] are 0.0184 in. (0.314δ) and 0.00162 in. (0.028δ), respectively. The number of time steps used per period of the disturbance function was 600. Each of the computations discussed below were carried out for at least 16 periods before the data were analysed. Three iterations were performed at each time step to obtain second-order accuracy in time.

The grid and domain parameters, time-step value, and number of iterations per time-step mentioned above are for the nominal case for which results are presented in this section. However, several other tests were performed to check the invariance of the solution to computational parameters. These tests are outlined below:

1. A grid refinement in the x and y directions.
2. An increase in the value of the time-step by a factor of 2.
3. A decrease in channel width by a factor 10.
4. A variation of the number of iterations per time-step between 2 and 4.

All of these tests resulted in very small changes in the solution indicating that the results presented below are independent of the grid and time-step chosen. The third test demonstrates that the mean acceleration in the channel

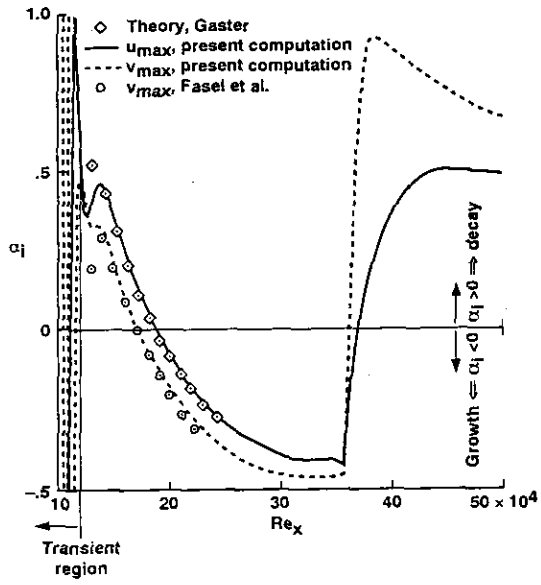

FIG. 3. Variation of growth rate α_i with Re_x.

is negligible for the channel width chosen and that the boundary layer very closely approximates a Blasius boundary layer (in addition, profiles of the streamwise and wall-normal mean-velocity components were found to be nearly identical to those of the Blasius boundary layer in the near-wall region).

The growth rate α_i for both the u and v components of velocity is shown plotted as a function of Re_x in Fig. 3. Included in this figure are the results of Gaster (as reported in Ref. [5]) and the numerical results of Ref. [5] for the v component of velocity. The values of α_i in both this investigation and Ref. [5] were obtained using the maximum amplitude at each streamwise location. The values of α_i for the u component are in good agreement with the theory of Gaster (a similar agreement for this component is reported in Ref. [5]). The values of α_i for the v component are in good agreement with those of Ref. [5]. Both the present computations and those of Ref. [5] show growth near the blowing/suction strip followed by a region of decay ($\alpha_i > 0$) and a second region of growth ($\alpha_i < 0$). In addition, in the present computation very large decay rates are seen in the coarse-grid region $Re_x \geq 35.0 \times 10^4$; this helps attenuate the disturbances such that the effect of the exit pressure reflective boundary condition is negligible. It should be noted that both the present computation and that of Ref. [5] show different growth rates for the u and v components.

Figure 4 shows the variation of α_r (the wave number in the streamwise direction) for the v component with Re_x. Included in this figure are the data from the present computation, data from [5], and results from linear theory. The difference between the different results in the post transition region is less than 2.0%.

The u and v amplitude distributions in the wall-normal direction at the location $Re_x = 152{,}400$ are shown in Fig. 5. The computed data of the present investigation are compared with linear theory. Clearly the two sets of data are in good agreement. Figure 6 shows a similar comparison of velocity amplitudes at the streamwise location $Re_x = 355{,}600$.

The integration scheme used is iterative-implicit in nature and requires multiple iterations at each time-step to be time-accurate. Strict second-order accuracy in time is achieved only when the residual $(Q^{p+1} - Q^p)$ is driven to zero at each time step. However, in practice, a moderate drop in residual values has been found to yield time-varying solutions that are essentially independent of additional iterations. Figure 7 shows the variation of the growth factor α_i with Re_x obtained with 2, 3, and 4 iterations per time step. Two iterations yielded an rms residual reduction of about 12, three iterations yielded a reduction of about 125, and

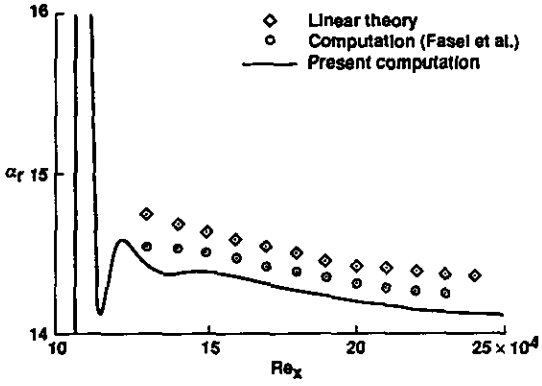

FIG. 4. Variation of streamwise wavenumber with Re_x.

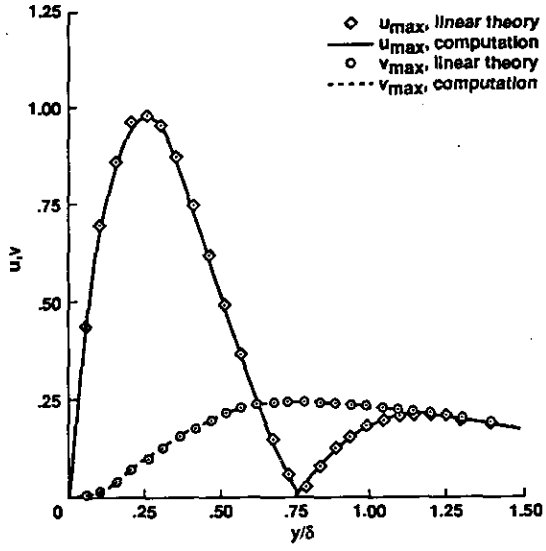

FIG. 5. Amplitude distributions in the wall-normal direction at $Re_x = 152{,}400$.

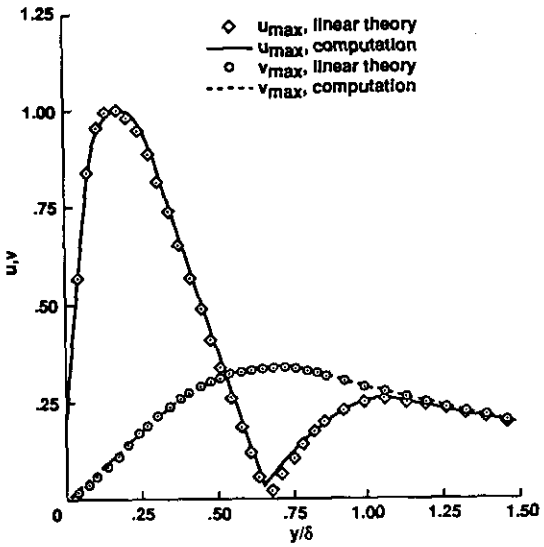

FIG. 6. Amplitude distributions in the wall-normal direction at $Re_x = 355{,}600$.

four iterations yielded a reduction in residual of about 470. The solution obtained with two iterations per time-step

growth of small amplitude disturbances using both zones 2 and 3 with zone 3 containing twice the mesh density of zone 2 have revealed oscillations in α_i in the immediate vicinity of the zonal boundary. However, the corresponding errors in the amplitudes were negligible. The oscillations in α_i have been found to be caused by the lower-order-accurate difference formulations used at grid points near the zonal boundary (in the x direction). The use of higher-order-accurate difference formulations at near-boundary points resulted in negligible oscillations in α_i. The development of such high-order-accurate difference formulations is described in Ref. 17.

RESULTS

In this section, results obtained for the flat-plate flow are presented. These results were computed by integrating the governing equations in conjunction with the natural and zonal boundary conditions described in the previous sections. Three iterations were performed at each time step. The root-mean-square residual decreased by a factor of about 15 at the end of the third iteration in zone 3 (which contains the finest grid) and by a factor of about 200 in

zone 1 as 10 in., that of zone 2 as 21 in., the well-resolved portion of zone 3 as 3 in., and the exit region (with the rapidly coarsening grid) as 12 in. The grid system consisted of a $(101 \times 51 \times 181)$ grid in zone 1, a $(842 \times 61 \times 181)$ grid in zone 2, and a $(271 \times 71 \times 361)$ grid in zone 3. The total number of grid points used was 17,357,664. The grid B computation ws performed with the length of zone 1 as 10 in., that of zone 2 as 7.25 in., the well-resolved portion of zone 3 as 5.75 in., and the exit region as 12 in. The grid system consisted of a $(101 \times 61 \times 181)$ grid in zone 1, a $(292 \times 61 \times 181)$ grid in zone 2, and a $(493 \times 71 \times 361)$ grid in zone 3. The total number of grid points used was 16,975,196. The spanwise dimension of the computational region for both grids A and B was $\pi/2$ in. (this was estimated using the spanwise dimension requirement of the channel-flow computations of Ref. [10]). Figure 2 shows the lengths of zones 1–3 used in grids A and B and also the resolution in the streamwise and spanwise directions (based on the wall shear velocity at $\mathrm{Re}_x = 650{,}000$).

The height of the computational box is 3.0 in. Since symmetry boundary conditions are used on the upper boundary of all the zones, the simulation is in effect a channel-flow simulation, albeit a very wide channel (approximately 130 times the momentum thickness at $\mathrm{Re}_x = 12.0 \times 10^5$). The resulting acceleration of the flow is minimal, the acceleration parameter K ($K = (\nu\, du/dx)/u^2$) being approximately 1.6×10^{-8}. Hence, the onset and length of transition are essentially the same as those for the zero-acceleration case.

The nondimensional time-step used in the computation was $\Delta t u_\infty/\delta^* = 0.044$, where δ^* is the displacement boundary-layer thickness at the end of the well-resolved portion of zone 3 in grid B (at $\mathrm{Re}_x = 6.5 \times 10^5$). The maximum CFL number corresponding to this time-step is about 60.0 (the CFL number based on the convective velocity is approximately 6.0). The integration time used for the accumulation of the statistical sample presented in this study (grid B) is approximately $175\delta^*/u_\infty$. The computing time required to obtain this sample was about 800 h on a Cray-YMP. The computer program required about 14 μsec of CPU time per grid point per iteration.

Characterization of Free-Stream Disturbance

As described in the previous section the free-stream disturbance is generated by perturbing the three velocity components at the inlet of zone 1. The inlet perturbation velocities are obtained using a prescribed power spectrum (these data were taken from Refs. [7–9]). The length scale Λ was taken to be 0.5 in. However, the disturbance characteristics obtained at the leading edge of the plate are different from those specified at the inlet. In this study, the intensity values at the inlet of zone 1 were iteratively modified until the intensity values at the leading edge of the plate were approximately the same as those obtained in Refs. [7–9] (labeled as the grid No. 2 case in Refs. [7–9]).

Figure 8 shows the variation of u_{rms}, v_{rms}, w_{rms}, and the free-stream turbulence intensity (T_{rms}) at a height of 0.5 in above the flat plate. An inlet intensity value of 9% (of the free-stream velocity) was used for all the velocity components in order to obtain intensity values around 2.75% at the leading edge of the plate (Ref. [7] reports a value of 2.6% for the grid No. 2 case). Note in Fig. 8 that the three components converge to nearly the same value at the leading edge of the plate. The experimental data of Ref. [7] show a variation of $\pm 15.0\%$ in intensity values at the leading edge with $v_{\mathrm{rms}} > w_{\mathrm{rms}} > u_{\mathrm{rms}}$.

Figure 9 shows the power spectrum obtained 1.0 in. upstream of the leading edge and 0.5 in. above the flat plate

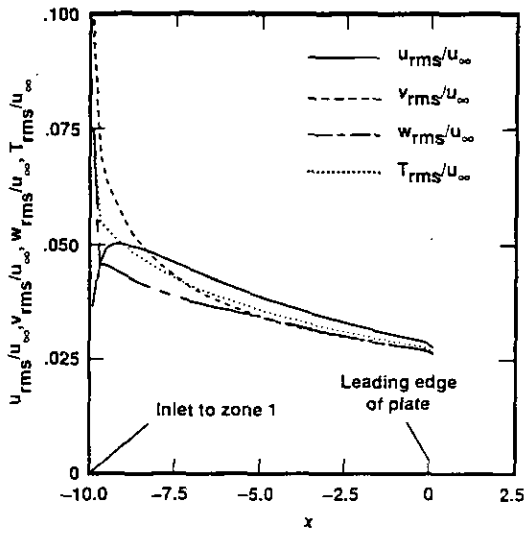

FIG. 8. Variation of free-stream turbulence intensities in zone 1 at $y = 0.5$.

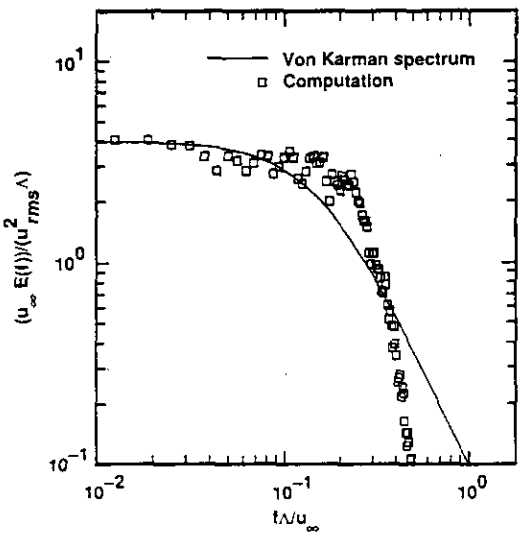

FIG. 9. Computed power spectrum for the streamwise velocity component, 1.0 in. upstream of the leading edge and at $y = 0.5$ in.

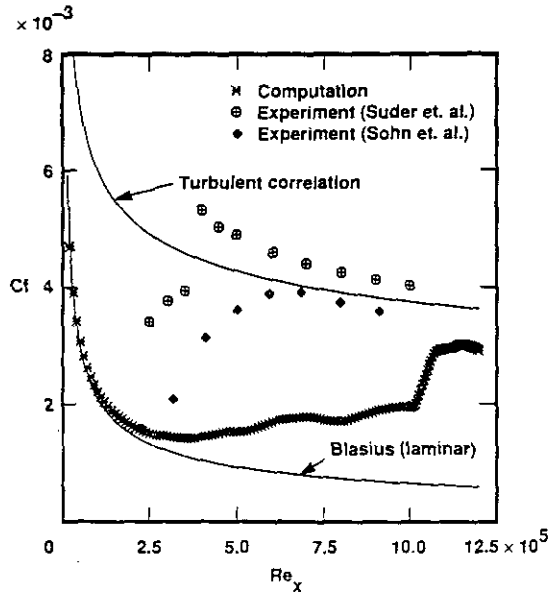

FIG. 10. Computed skin friction along the length of the flat plate (coarse grid).

for the streamwise component of the velocity. This power spectrum was computed using fast Fourier transforms (FFTs) in conjunction with a Hanning window, as was done in Ref. 19. The size of the window was chosen as the period of the lowest frequency perturbation introduced at the inlet to zone 1 (the lowest frequency being 24 Hz). Larger windows result in more noisy data. The computed spectrum roughly approximates the Von Karman spectrum. In a more recent investigation it was determined that the computed spectrum closely approximates the spectrum obtained in the late stages of decay of isotropic turbulence; the reason for this behavior as well as the modifications required in the computational procedure to obtain the Von Karman spectrum will be discussed in a separate article. The experimentally obtained power spectrum of Ref. [7] has not been reproduced in Fig. 9, because it closely matches the Von Karman spectrum in the frequency range depicted.

Surface Skin-Friction Comparisons

To the applied computational fluid dynamicist, surface skin-friction and heat transfer are important variables that cannot be predicted accurately and reliably using the Reynolds-averaged Navier–Stokes equations and the available turbulence models. Hence, we place particular emphasis on the computed skin friction in this study.

Figure 10 shows the computed skin-friction, the experimental data from Refs. [8, 9], and the laminar and turbulent (turbulent correlation from Ref. [18]) skin-friction distributions. The experimental configuration of Ref. [9] is nearly identical to that of Ref. [8] except that the experiments were conducted with a heated wall instead of an adiabatic wall. The computed data shown in Fig. [10] were obtained on an extremely coarse grid ($101 \times 51 \times 61$) in zone 1, ($402 \times 51 \times 61$) in zone 2, and ($185 \times 61 \times 121$) in zone 3. The computed data do show an increase in skin friction over the laminar values, and this increase is seen to originate in the region where the experimental data indicate the onset of transition. The increased resolution in zone 3 (twice that of zone 2 in the x and z directions and near the wall in the y direction) results in a very rapid increase in skin friction at about $Re_x = 10 \times 10^5$. However, both the zone 2 and zone 3 skin-friction values fall far short of the values obtained from the turbulent correlation as well as the experimental data. This is to be expected because of the coarse grids used in zones 2 and 3. One point of computa-

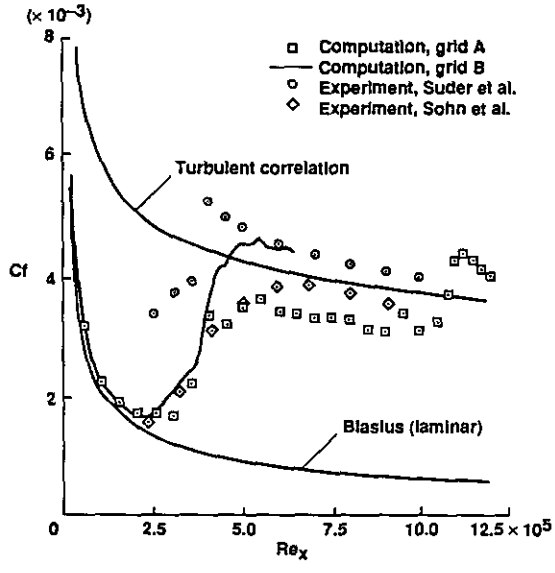

FIG. 11. Computed skin friction along the length of the flat plate (grids A and B).

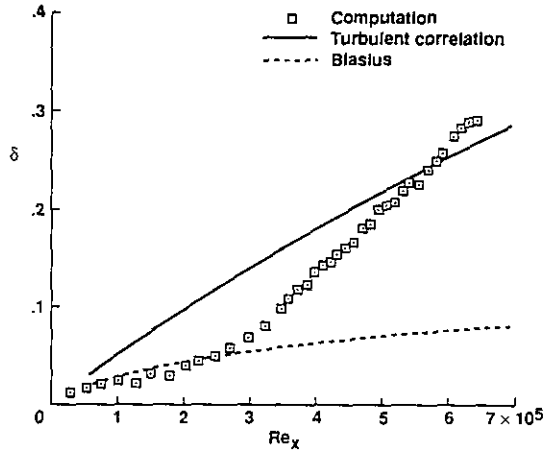

FIG. 12. Variation of boundary-layer thickness with streamwise distance.

tional interest is the smooth transition of the skin friction in the zonal boundary region (which is at $Re_x = 10 \times 10^5$ for this computation).

Figure 11 shows the skin-friction variation as in Fig. 10 but from the computations on grids A and B. The improvement in the computed skin friction is apparent. The computed onset of transition coincides well with the experimental onset of transition in both computations. The grid A curve levels off at a lower value (because of the coarser grid in zone 2) and subsequently, in zone 3, the computed skin friction overshoots the turbulent correlation and then decreases. This overshoot has been observed in other experiments at high free-stream turbulence levels. However, the overshoot in the computation occurs at a point where the grid resolution is increased—not near the experimentally observed transition region. Both Figs. 10

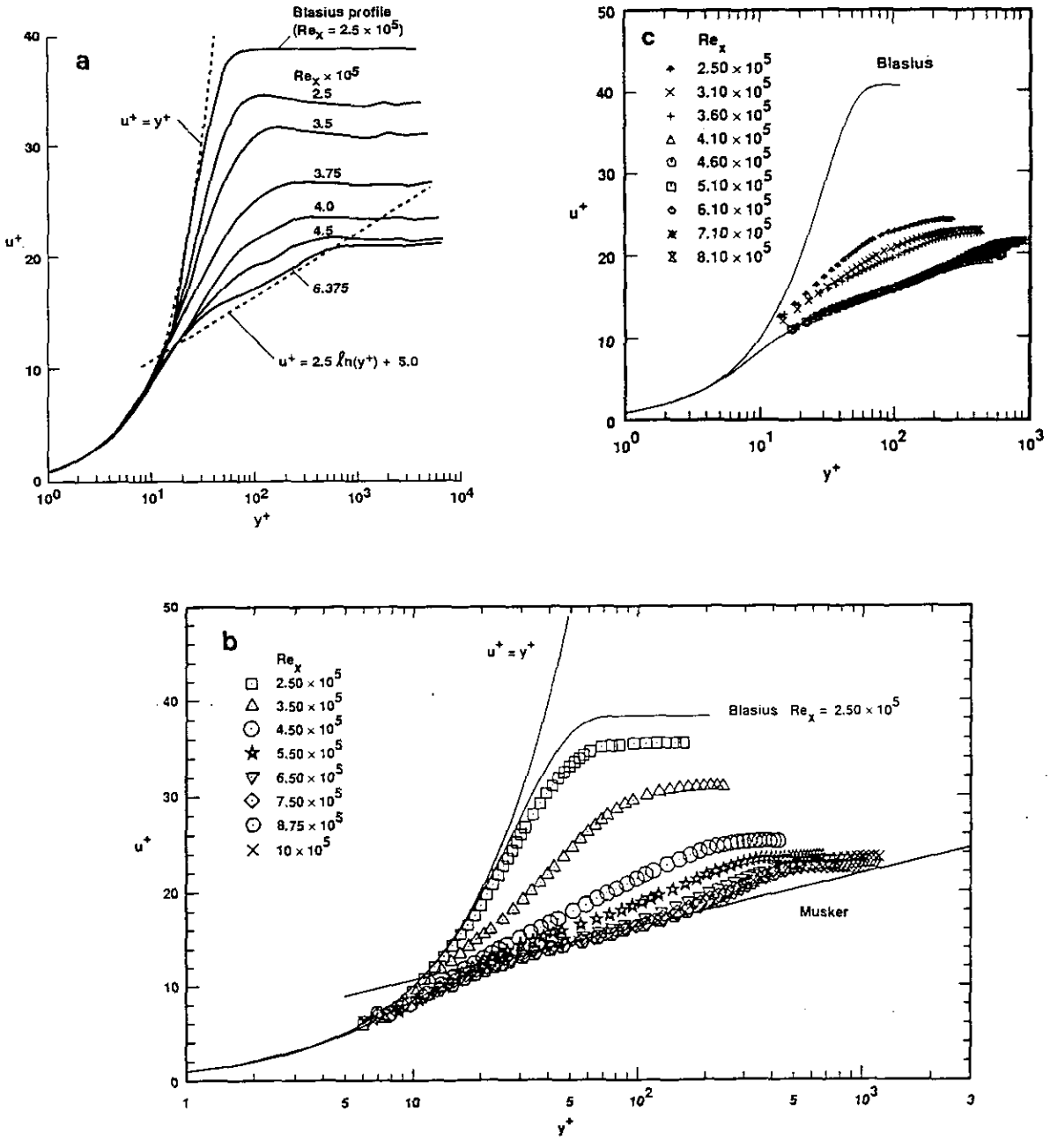

FIG. 13. Mean velocity profiles normalized by wall-shear velocity at various streamwise locations: (a) computed profiles; (b) experimental profiles (Ref. [9]); (c) experimental profiles (Ref. [8]).

and 11 indicate a second "numerical transition" in the region where the grid resolution increases. The grid B curve shows a transition region that lies in between the data from Refs. [8, 9]. The well-resolved region in zone 3 is not sufficiently long to determine if the computed skin friction reduces in value to the turbulent correlation farther downstream. The presence of small oscillations in the skin-friction data is a reflection of a marginal statistical sample. Smoother data can be obtained by using a larger sample.

Velocity Statistics

In this subsection we present some of the velocity data obtained in the transition region and in the early-turbulent region. Only the results obtained from the grid B computation are included here. In many of the figures cited herein, the wall-normal direction (y) is nondimensionalized by the local boundary-layer thickness. Figure 12 shows the variation of the boundary-layer thickness in the streamwise

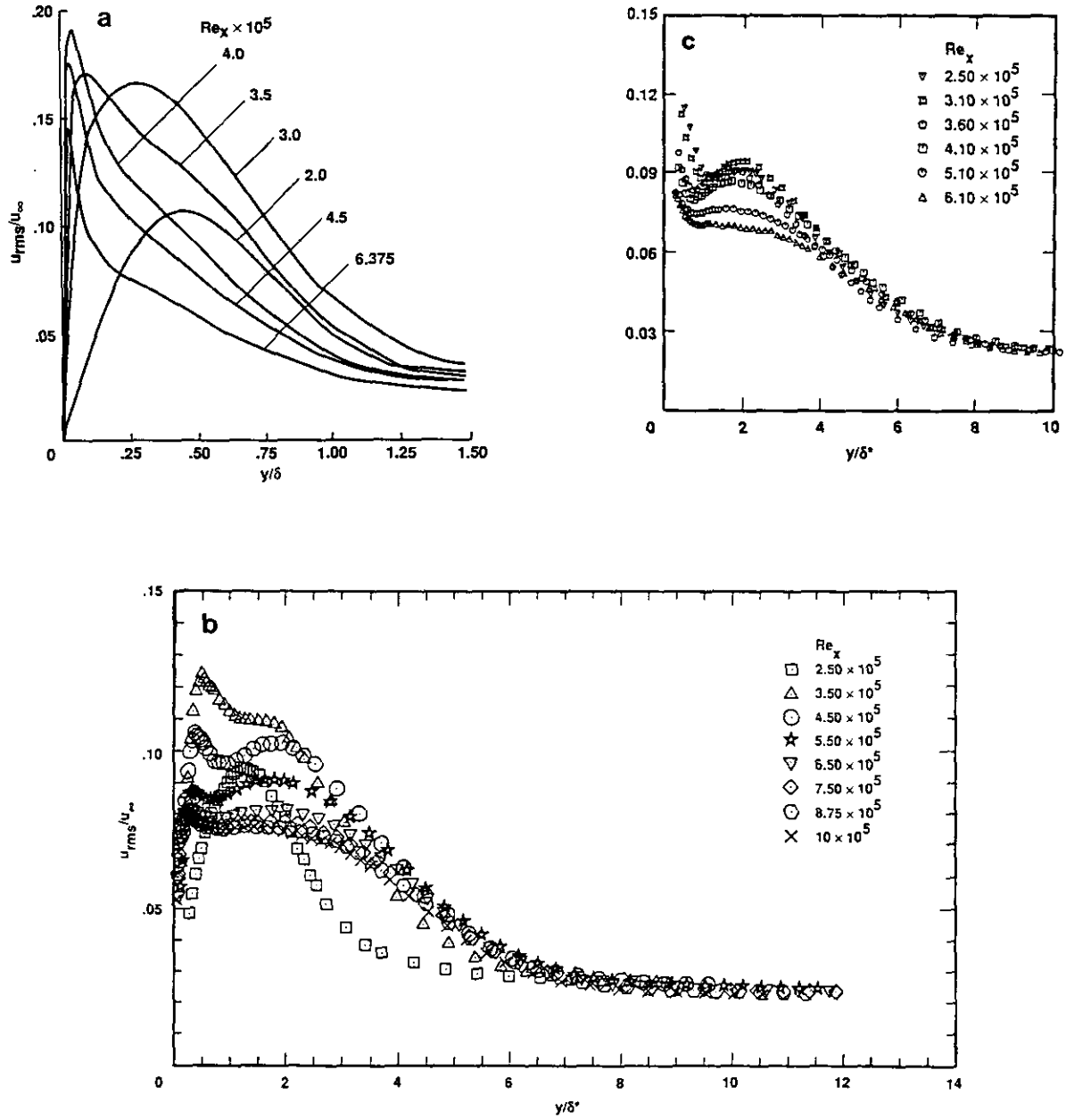

FIG. 14. Streamwise component of turbulence intensity at various streamwise locations (normalized by free-stream velocity): (a) computed profile; (b) experimental profile (Ref. [9]); (c) experimental profile (Ref. [8]).

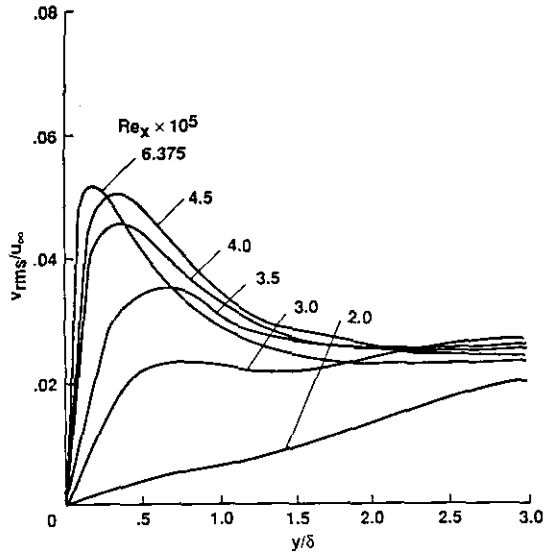

FIG. 15. Computed normal component of turbulence intensity at various streamwise locations (normalized by free-stream velocity).

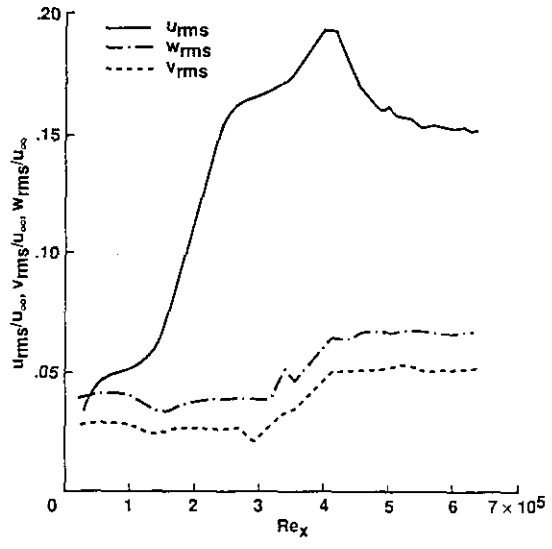

FIG. 17. Variation of peak turbulence intensities with streamwise distance.

direction. Included in this figure are the laminar boundary-layer thickness and the turbulent boundary-layer thickness obtained from a turbulent correlation [18].

Figure 13a shows computed mean velocity profiles obtained at various streamwise locations. The dashed lines represent the law of the wall and the log law $[u^+ = 2.5 \ln(y^+) + 5.0]$. The laminar velocity profile at $Re_x = 2.5 \times 10^5$ is also shown. The computed velocities gradually change from laminar to the turbulent profile with increasing Re_x. The changes in the velocity profiles are more rapid in the transition region than in the early turbulent region. Similar trends are seen in the data of Ref. [9], shown in Fig. 13b, and those of Ref. [8], shown in Fig. 13c. Turbulent profiles are attained earlier in Fig. 13c than in Fig. 13b. This observation is consistent with the behavior of the corresponding skin-friction profiles shown in Fig. 11. The computed profiles indicate a transition region that lies between the two sets of experimental data.

The computed turbulent profile $(Re_x = 6.375 \times 10^5)$ satisfies the law of the wall but does not duplicate the log law well. The reason for the discrepancy is that the resolution in zone 3 is less than that required for an accurate

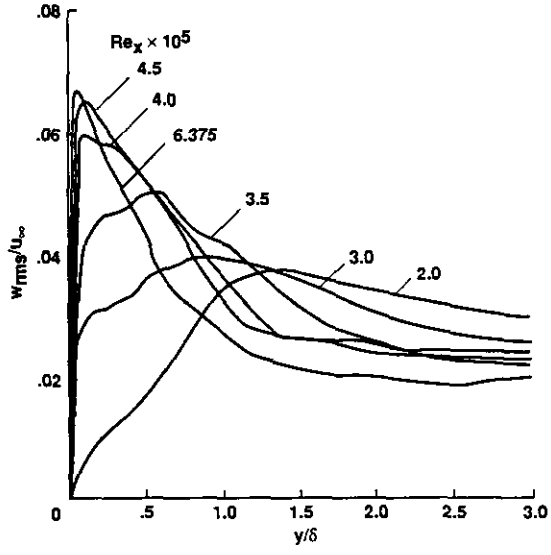

FIG. 16. Computed spanwise component of turbulence intensity at various streamwise locations (normalized by free-stream velocity).

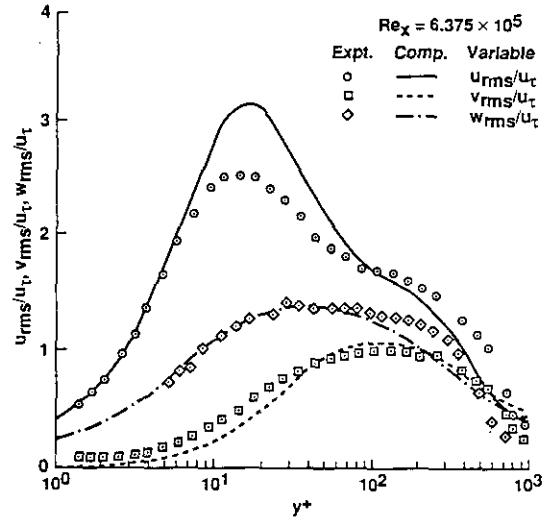

FIG. 18. Turbulence intensities at streamwise location $Re_x = 6.375 \times 10^5$, normalized by wall-shear velocity and plotted in wall coordinates.

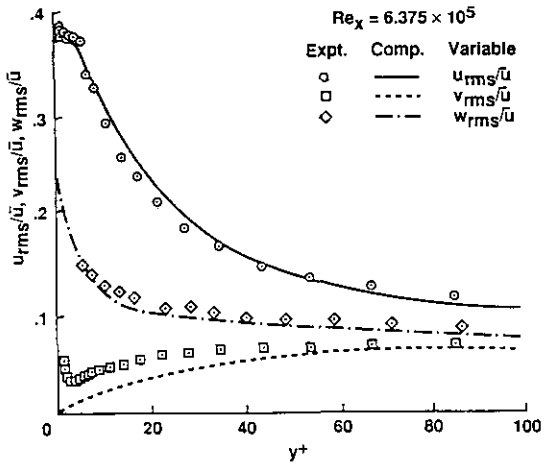

FIG. 19. Turbulence intensities at streamwise location $Re_x = 6.375 \times 10^5$, normalized by local mean velocity and plotted in wall coordinates.

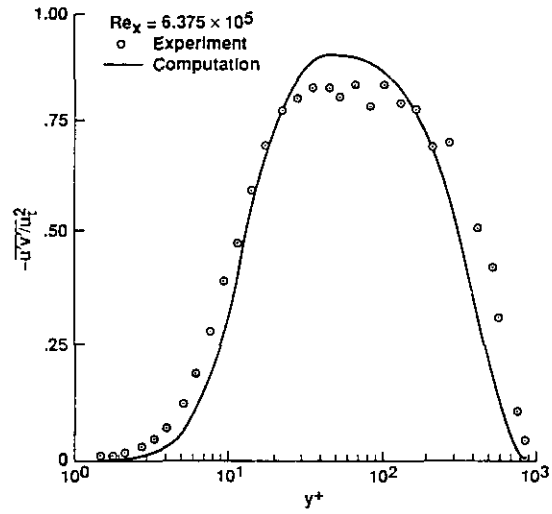

FIG. 21. Reynolds shear–stress distribution at the streamwise location $Re_x = 6.375 \times 10^5$, normalized by the square of the wall-shear velocity and plotted in wall coordinates.

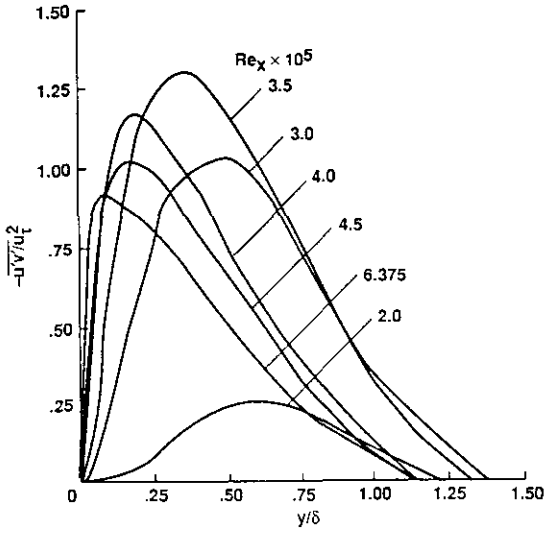

FIG. 20. Reynolds shear–stress distributions at various streamwise locations, normalized by the square of the wall-shear velocity.

simulation of turbulent flow. The channel-flow results of Ref. [10] indicate that the grid spacings in the x and z directions that are required for an accurate simulation are $\Delta x^+ \simeq 12.0$ and $\Delta z^+ \simeq 6.0$. Accurate computations of transition may require an even higher resolution. The values used in this study in zone 3 (based on the wall-shear velocity at $Re_x = 6.5 \times 10^5$) are $\Delta x^+ \simeq 28.2$ and $\Delta z^+ \simeq 9.8$. A mesh refinement study is far too expensive on currently available computers. However, computations on coarser meshes, such as the one on which the data of Fig. 10 were obtained, resulted in a larger discrepancy between the computed results and the log law.

Figure 14a shows the streamwise component u_{rms} of the turbulence intensity normalized by the free-stream velocity at various locations along the plate: in the transition region ($Re_x = 2.0, 3.0, 3.5, 4.0, 4.5 \times 10^5$) and in the early turbulent region ($Re_x = 6.375 \times 10^5$). The peak value increases with increasing Re_x and reaches its maximum (about 18.5% of the free-stream velocity) at about $Re_x = 4.0 \times 10^5$ in the

FIG. 22. Spanwise vorticity contours in an (x, y) plane in the region $2.0 \times 10^5 \leqslant Re_x \leqslant 3.5 \times 10^5$ at $t = 20.5\delta^*/u_\infty$.

FIG. 23. Spanwise vorticity contours in an (x, y) plane in the region $2.25 \times 10^5 \leqslant Re_x \leqslant 3.75 \times 10^5$ at $t = 41.0\delta^*/u_\infty$.

FIG. 24. Spanwise vorticity contours in an (x, y) plane in the region $2.5 \times 10^5 \leqslant Re_x \leqslant 4.0 \times 10^5$ at $t = 51.25\delta^*/u_\infty$.

FIG. 25. Spanwise vorticity contours in an (x, y) plane in the region $2.5 \times 10^5 \leqslant Re_x \leqslant 4.0 \times 10^5$ at $t = 61.5\delta^*/u_\infty$.

FIG. 26. Spanwise vorticity contours in an (x, z) plane at $y^+ = 4.5$ and in region $2.25 \times 10^5 \leqslant Re_x \leqslant 3.75 \times 10^5$.

FIG. 27. Spanwise vorticity contours in an (x, z) plane at $y^+ = 4.5$ and in region $3.625 \times 10^5 \leqslant Re_x \leqslant 5.125 \times 10^5$.

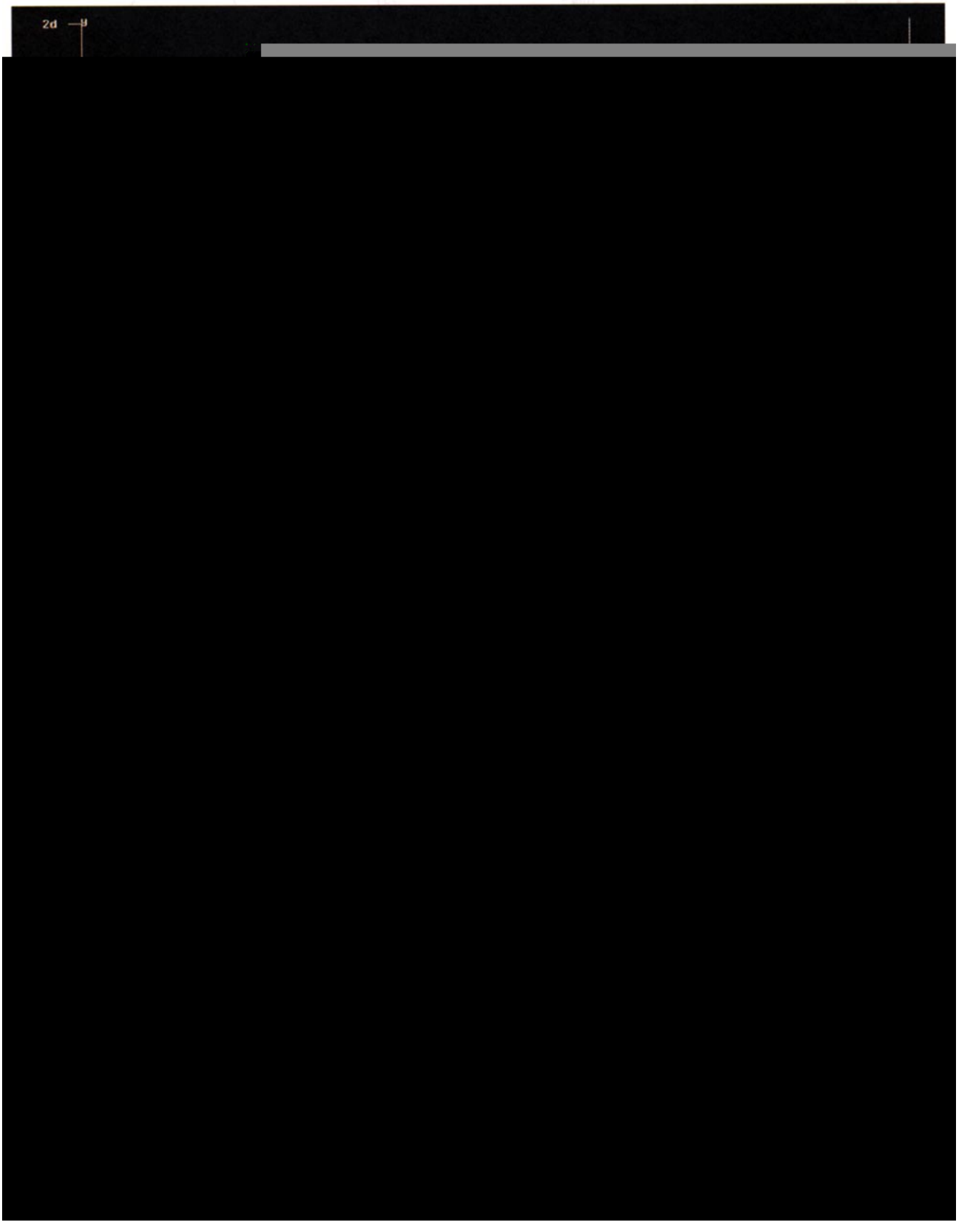
2d

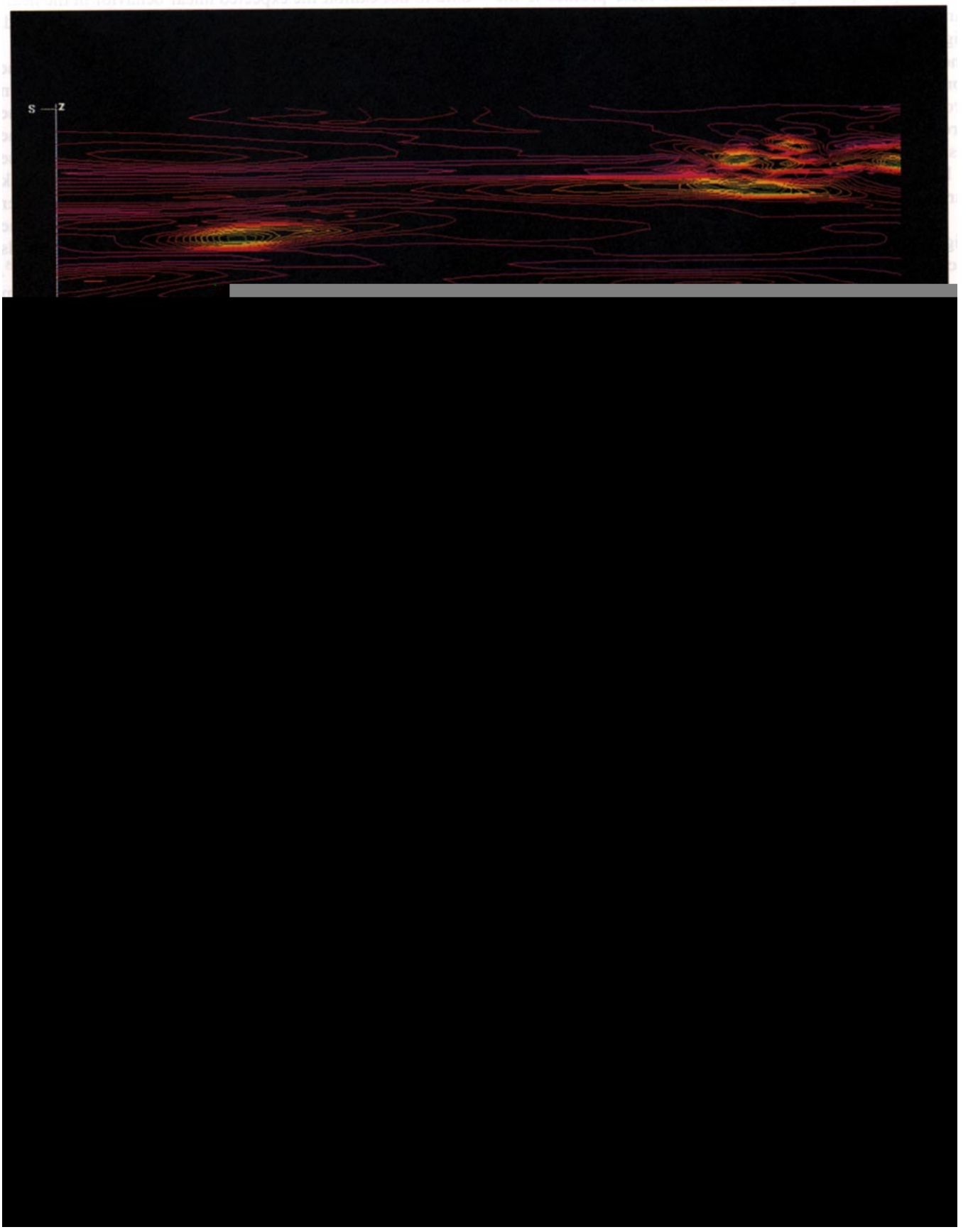
S
Z

transitional region. Thereafter it decreases to about 14% of the free-stream velocity in the turbulent region. The location of the peak value is seen to move closer to the wall with increasing Re_x. The general trend of these profiles is the same as that observed in Ref. [9], which is shown in Fig. 14b, and in Ref. [8], which is shown Fig. 14c. However, is very nearly the same as the experimental value of 0.39. The normal component is lower than that of the experimental data. It should be noted that the experimental $v_{rms}/\bar{u}$ data to not exhibit the expected linear behavior in the near-wall region; instead, they increase as the wall is approached, thus indicating experimental errors.

in the region $3.625 \times 10^5 \leqslant \mathrm{Re}_x \leqslant 5.125 \times 10^5$. The transition process is essentially completed in this region. The appearance of the vortical structures, which occurs at about $\mathrm{Re}_x = 4.0 \times 10^5$ is very abrupt. There are only a few such structures upstream of this streamwise location. In animations of the spanwise vorticity cntours in this region, some of these structures were seen to originate as extremely small, approximately circular regions of concentrated vorticity which then elongate into the larger elliptical shapes seen in Fig. 27. Some of these early, less elongated shapes can be seen in the upstream region.

Figure 28 shows spanwise vorticity contours in the (x, z) plane in the early turbulent region, $5.0 \times 10^5 \leqslant \mathrm{Re}_x \leqslant 6.5 \times 10^5$. Unlike in Fig. 27, the vortical structures fill the entire region and a certain pattern uniformity is observed. Figure 29 shows spanwise contours in the exit region where the grid rapidly expands. The dissipation of spanwise vorticity owing to grid coarseness is evident (thus validating the use of the exit boundary procedure discussed earlier).

Streamwise vorticity contours in the region $3.625 \times 10^5 \leqslant \mathrm{Re}_x \leqslant 5.125 \times 10^5$ are shown in Fig. 30 at $y^+ = 34.5$. The irregular boundary seen in Fig. 30, closely resembles that of Fig. 27. Figures 31 and 32 also show streamwise vorticity contours, but in regions that are subsets (both in the streamwise and spanwise directions) of the region shown in Fig. 30. The letter "s," used to mark the ordinate, represents the dimension of the computational region in the z direction ($\pi/2$ in.). One important feature that has been noticed is that the transition boundary is marked by the appearance of counterrotating vortex pairs (clearly evident in Fig. 32). Figure 33 shows crossflow velocity vectors in a (y, z) plane that is located approximately in the middle of Fig. 32, thus cutting through the largest pair of vortices. The cross-sectional structure of this pair of vortices is clearly seen in Fig. 33. The letter "d," used to mark the ordinate in Fig. 33, represents the laminar boundary-layer thickness at $\mathrm{Re}_x = 4.0 \times 10^5$. The wall-normal extent of the vortex pair is about one boundary-layer thickness.

SUMMARY

A direct simulation of transition and turbulence in a spatially evolving boundary layer is described. The simulation is performed using a high-order-accurate, upwind-biased, iterative-implicit, finite-difference algorithm. The algorithm is developed for the unsteady, compressible form of the Navier–Stokes equations. However, the simulation is performed at a low subsonic Mach number (0.1) because experimental data are available for this speed regime. This study focuses on the high-free-stream disturbance case in which transition to turbulence occurs close to the leading edge, thereby substantially reducing computing requirements. A method of numerically generating free-stream disturbances of a prescribed nature is also presented.

One numerical tool that has been extremely useful in the current investigation is the multiple-zone technique, which permits the use of different grid densities in different regions of the flow. The multiple-zone approach has resulted in an efficient use of the total number of grid points available. The zoning technique has been used in the current study to reduce the number of grid points in zones 1 and 2. It was found that the zonal procedure did not degrade the quality of the solution in the vicinity of the zonal boundary.

Results included (1) the variation of skin friction along the length of the flat plate, (2) velocity-related statistical data, and (3) preliminary visualizations of the instantaneous flow field to elucidate the nature of the computed transition process. Specifically, it was shown that the transition boundary was marked by pairs of counterrotating streamwise vortices. Comparisons with experimental data are also included. The results indicate that the essential observed features of the transition process have been captured in the computation. However, earlier channel-flow computations, as well as grid refinement studies in this investigation, indicate that a grid that is finer by as much as factors of 2.0 and 1.5 in the streamwise and spanwise directions, respectively, may be required to achieve an accurate simulation.

FIG. 28. Spanwise vorticity contours in an (x, z) plane at $y^+ = 4.5$ and in region $5.0 \times 10^5 \leqslant \mathrm{Re}_x \leqslant 6.5 \times 10^5$.

FIG. 29. Spanwise vorticity contours in an (x, z) plane at $y^+ = 4.5$ and in region $6.5 \times 10^5 \leqslant \mathrm{Re}_x \leqslant 12.5 \times 10^5$.

FIG. 30. Streamwise vorticity contours in an (x, z) plane at $y^+ = 34.5$ and in region $3.625 \times 10^5 \leqslant \mathrm{Re}_x \leqslant 5.125 \times 10^5$ and $0 \leqslant z \leqslant s$.

FIG. 31. Streamwise vorticity contours in an (x, z) plane at $y^+ = 34.5$ and in region $3.625 \times 10^5 \leqslant \mathrm{Re}_x \leqslant 4.625 \times 10^5$ and $s/3 \leqslant z \leqslant 2s/3$.

FIG. 32. Streamwise vorticity contours in an (x, z) plane at $y^+ = 34.5$ and in region $3.625 \times 10^5 \leqslant \mathrm{Re}_x \leqslant 4.0 \times 10^5$ and $s/3 \leqslant z \leqslant s/2$.

FIG. 33. Crossflow velocity vectors at the streamwise location $\mathrm{Re}_x = 384{,}375$.

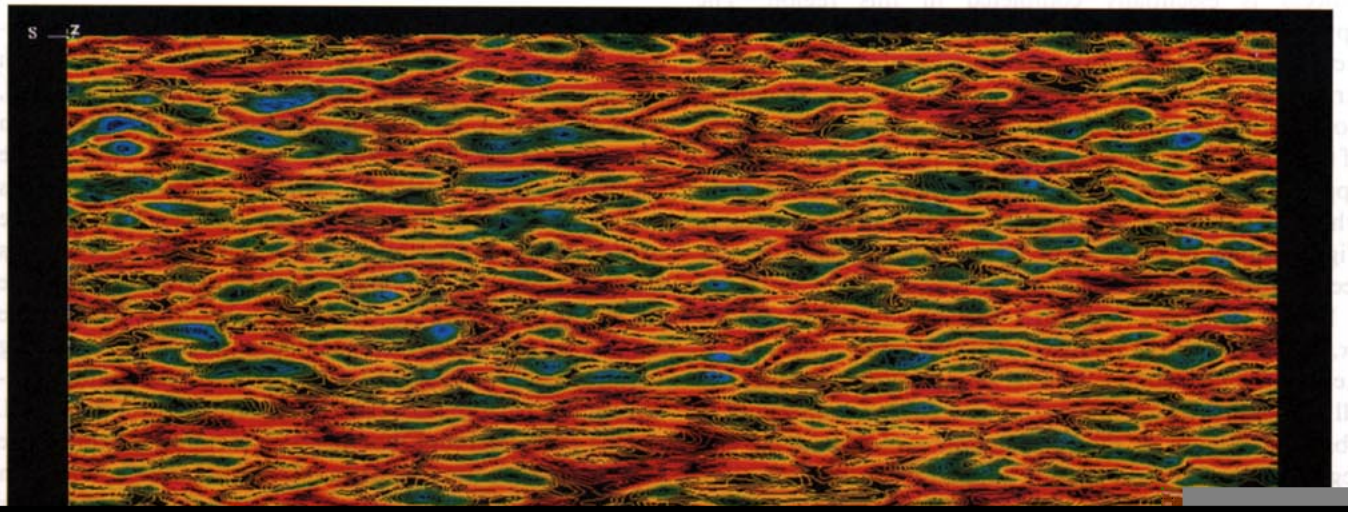
S
Z

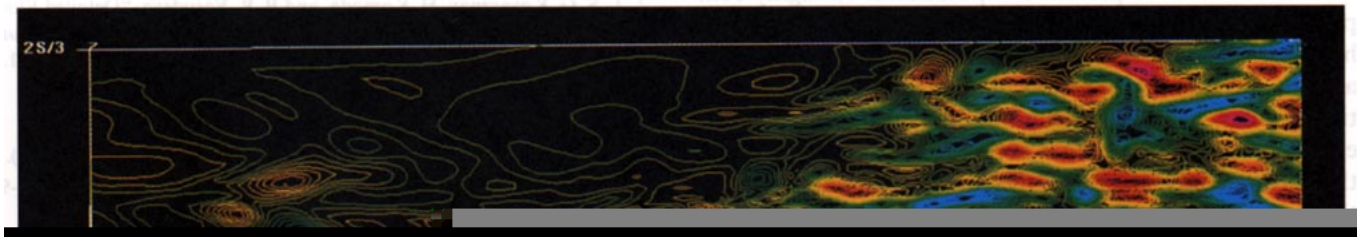
2S/3

Computing times for the flow field under investigation are several hundred hours per case on a Cray-YMP (the sample obtained for the grid B computation required 800 h). One of the reasons that the present computation is so highly computation-intensive is the low free-stream Mach number that has been used. The large disparity between the fluid velocity and the speed of sound results in an extremely slow integration process. At higher Mach numbers (0.4 and above) the estimated computing time is about 25% of that required in the current study. However, the current study does indicate that computing transition and turbulence in a spatially evolving boundary layer to a reasonable degree of accuracy

REFERENCES

1. A. Wray and M. Y. Hussaini, *Proc. R. Soc. London Ser. A* **392**, 373 (1984).
2. L. S. G. Kovasznay, H. Komoda, and B. R. Vasudeva, "Detailed Flow Field in Transition," in *Proceedings, 1962 Heat Transfer and Fluid Mechanics Institute* (Stanford Univ. Press, Stanford, CA, 1962), p. 1.
3. P. R. Spalart and K.-S. Yang, *J. Fluid Mech.* **178**, 345 (1987).
4. E. Laurien and L. Kleiser, *J. Fluid Mech.* **199**, 403 (1989).
5. H. F. Fasel, U. Rist, and U. Konzelmann, *AIAA J.* **28**, No. 1 (1990).
6. T. A. Zang, S. E. Krist, and M. Y. Hussaini, ICASE Report No. 89-9, 1989 (unpublished).
7. M. F. Blair, *ASME J. Heat Transf.* **105**, 33 (1983).